Available online at www.sciencedirect.com

ScienceDirect

www.elsevier.com/locate/jmbbm

Research Paper

Mechanical behaviour of a fibrous scaffold for ligament tissue engineering: Finite elements analysis *vs.* X-ray tomography imaging

Cédric P. Laurent[a,*], *Pierre Latil*[b,c], *Damien Durville*[d], *Rachid Rahouadj*[a], *Christian Geindreau*[b,c], *Laurent Orgéas*[b,c], *Jean-François Ganghoffer*[a]

[a]CNRS, LEMTA, UMR 7563, Université de Lorraine, 2 avenue de la forêt de Haye, 54502 Vandoeuvre-lès-Nancy, France
[b]CNRS, 3SR Lab, F-38000 Grenoble, France
[c]Univ. Grenoble Alpes, 3SR Lab, F-38000 Grenoble, France
[d]CNRS, MSSMat, UMR 8579, Ecole Centrale Paris, Grande Voie des Vignes, 92290 Chatenay-Malabry, France

ARTICLE INFO

Article history:
Received 12 May 2014
Received in revised form
25 August 2014
Accepted 2 September 2014
Available online 16 September 2014

Keywords:
Ligament tissue engineering
Braided biodegradable polymer scaffold
Finite element analysis
X-ray microtomography

ABSTRACT

The use of biodegradable scaffolds seeded with cells in order to regenerate functional tissue-engineered substitutes offers interesting alternative to common medical approaches for ligament repair. Particularly, finite element (FE) method enables the ability to predict and optimise both the macroscopic behaviour of these scaffolds and the local mechanic signals that control the cell activity. In this study, we investigate the ability of a dedicated FE code to predict the geometrical evolution of a new braided and biodegradable polymer scaffold for ligament tissue engineering by comparing scaffold geometries issued from FE simulations and from X-ray tomographic imaging during a tensile test. Moreover, we compare two types of FE simulations the initial geometries of which are issued either from X-ray imaging or from a computed idealised configuration. We report that the dedicated FE simulations from an idealised reference configuration can be reasonably used in the future to predict the global and local mechanical behaviour of the braided scaffold. A valuable and original dialog between the fields of experimental and numerical characterisation of such fibrous media is thus achieved. In the future, this approach should enable to improve accurate characterisation of local and global behaviour of tissue-engineering scaffolds.

1. Introduction

Tissue engineering offers interesting alternative to common medical approaches for ligament and tendon repair (Butler et al., 2008; Leong et al., 2013; Vieira et al., 2009). This approach is based on the use of a biodegradable scaffold which must mimic the physiological function of the native tissue in one hand and encourage tissue regeneration in the second hand.

*Correspondence to: LEMTA, 2 avenue de la forêt de Haye, 54502 Vandoeuvre-lès-Nancy, France. Tel.: +33 3 83 59 55 81.
E-mail addresses: cedric.laurent@univ-lorraine.fr (C.P. Laurent), pierre.latil@3sr-grenoble.fr (P. Latil), damien.durville@ecp.fr (D. Durville), rachid.rahouadj@univ-lorraine.fr (R. Rahouadj), christian.geindreau@3sr-grenoble.fr (C. Geindreau), laurent.orgeas@3sr-grenoble.fr (L. Orgéas), jean-francois.ganghoffer@univ-lorraine.fr (J.-F. Ganghoffer).

http://dx.doi.org/10.1016/j.jmbbm.2014.09.003
1751-6161/

Among the different scaffolds that have been proposed, our team recently designed a new braided scaffold for anterior cruciate ligament tissue engineering (Laurent et al., 2011) which offers adapted tensile mechanical properties (Laurent et al., 2012) and an encouraging potential to be colonised by a biological tissue (Laurent et al., 2014). Particularly, this scaffold is well suited to a computer-aided tissue engineering approach (Laurent et al., 2013) enabling the numerical prediction and optimisation of both the scaffold properties and the cell's micro-environment that controls cellular activity (Rathbone et al., 2012; Skardal et al., 2013; Wang et al., 2005). Particularly, we have recently used a Finite Element (FE) code dedicated to fibrous materials (Durville, 2012) to predict the macroscopic mechanical response of this new scaffold and the local mechanical signals at the level of the cells (Laurent et al., 2012). Particularly, we used this code to compute Octahedral Shear Strains (*OSS*) at the scaffold surface: this quantity is thought to be a major mechanical signal for the cellular response (Lacroix et al., 2006). This FE code was used both to compute the initial braided configuration from an arbitrary idealised configuration and to successfully simulate the tensile response of the scaffold. However, the satisfying prediction of a macroscopic overall property such as the scaffold tensile response is not sufficient to draw definitive conclusions concerning the ability of the model to predict local mechanical and morphological cellular micro-environments. Consequently, the model ability to accurately predict the local geometry and mechanical stimuli at the scale of cells during a loading cycle still requires to be validated.

Substantial advances in X-ray microtomography of fibrous materials have been recently reported (Latil et al., 2011) and have been used to assess the performance of FE simulations of stent-graft severe bending (Demanget et al., 2012). A similar approach could be used to obtain an experimental description of fibres trajectories in the proposed braided scaffold from three-dimensional (3D) images, in order to compare experimental and numerical descriptions of scaffold geometry during a tensile test.

Consequently, the objective of the present contribution is to compare the 3D geometry of a real scaffold using X-ray microtomography with the geometry obtained by our FE simulations during a uniaxial loading–unloading test. Two different types of simulations were performed. For the first type, the scaffold geometry directly issued from 3D images before loading was used as the initial configuration of the FE simulation. For the second type, the simulations were carried out from an idealised description of the scaffold initial geometry. The ability of our computer-aided approach to bring information about cellular micro-environment when the scaffold is loaded was thus here assessed. Besides, this work constitutes and original dialog between the fields of experimental and numerical characterisation of fibrous media.

2. Materials and methods

2.1. Scaffold

The scaffold used in this study was presented in details in previous contributions (Laurent et al., 2012, 2011) as well as its corresponding manufacturing process. It was developed initially for anterior cruciate ligament tissue engineering, but may be largely adapted to other ligamentous or tendinous tissues. Briefly, it consists of a multilayer braided structure, each layer being made up of 16 fibres of poly(lactide-*co*-ε-caprolactone) in a ratio PLLA/PCL equal to 85/15. The fibres were processed using a custom setup enabling the plastic extrusion of small amounts of melted polymer with a controlled diameter (Laurent et al., 2011). This architecture and material were selected for the following reasons: (1) it is tailorable in terms of pore geometry and mechanical properties simply by varying the number of layers, the fibre diameter and the braiding angle, (2) it exhibits an anisotropic non-linear mechanical response, similar to ligamentous materials, (3) it offers a positive pore size gradient from the core to its periphery, which is suitable for nutriments circulation within the scaffold (Ahn et al., 2010), (4) it is biocompatible and slowly biodegradable, (5) its predictable geometry enables to adopt a "computer-aided tissue engineering" approach to simulate and optimise its characteristics. In the present study, a three-layer (*i.e.* with 48 fibres) scaffold with an external stress-free diameter of ≈ 5 mm was selected. In the following, the layers will be numbered from the core to the periphery of the scaffold, *i.e.* the third layer corresponds to the external layer.

2.2. X-ray microtomography

The method used to obtain deformed scaffold geometries is similar to the one described in previous studies (Demanget et al., 2012; Latil et al., 2011). Briefly, a laboratory X-ray microtomograph (3SR Lab, Grenoble, France, RX Solutions apparatus) was used. It consists of a microfocus enclosed tube (conical X-ray source, voltage from 40 to 150 kV, current intensity up to 500 μA) and a large detector (195.07×243 mm^2 with a field of view of 1920×1536 pixel). For the present experiments, the generator voltage and current intensity were respectively set to 100 kV and 100 μA. The acquisition rate was set to 5 images/s and 900 images were acquired on a 360° rotation allowing a rather short scanning time of about 20 min. The spatial resolution was such that each voxel had a size of $7.88 \times 7.88 \times 7.88$ μm^3. Lastly, the commercial reconstruction software DigiCT (Digisens, France) was used to obtain the 3D images of the scaffold from the 2D radiographs (Fig. 1).

To deform the scaffold, a custom experimental micro-press was used in order to subject the scaffold to a tensile loading inside the microtomography, as schematised in Fig. 1(a). The scaffold was mounted within clamps (initial gauge length ≈ 11.5 mm). Tensile strains were successively prescribed by controlling the distance between clamps using a piezoelectric motor (Piezomotor, Sweden) at a speed of 10 μm/s, while other displacements and rotations were locked due to the clamping system. The tensile forces associated with the prescribed strains were recorded by a miniature 50 N load cell (Measurement Specialties, United Kingdom) with a precision of around 0.1 N. Ten 3D images were obtained during the test: six during the loading, *i.e.* while the macroscale tensile force and Green–Lagrange strain respectively increased from 0.3 N to 32 N and from 0 to 0.04, and four during the scaffold unloading (see Fig. 1). Displacement steps were chosen in order to best describe the loading–unloading curve with a minimum number of steps, and each loading step was applied for around 5 min in order to

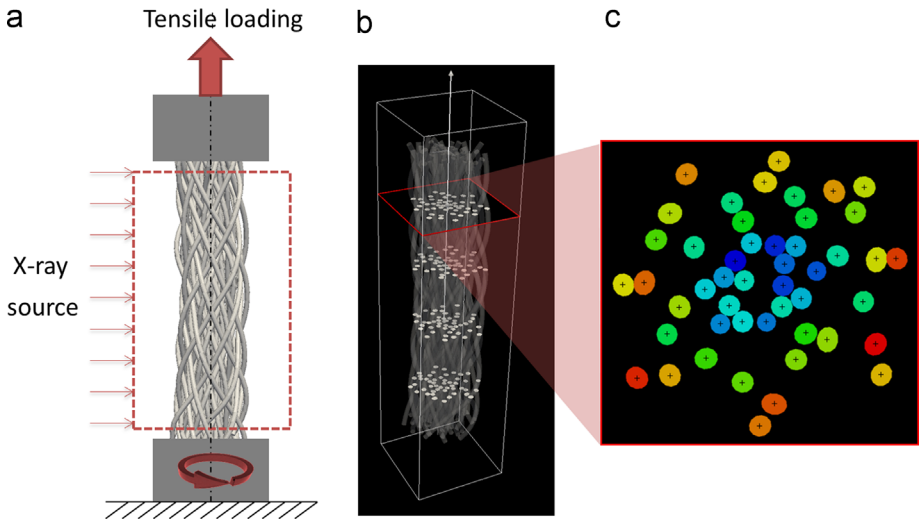

Fig. 1 – X-ray microtomography of the fibrous polymer scaffold. (a) Schematic representation of the experimental setup. (b) 3D reconstruction of the scaffold geometry. (c) Example of a slice of the 3D image, showing the image processing procedure aiming at extracting fibre centrelines.

image the scaffold geometry. Only the central part of the scaffold was reconstructed in order to limit the effect of the boundary conditions on the scaffold geometry (around 0.5 mm on each side were removed from the images).

The procedure used to analyse the resulting 3D images and to detect the fibres centrelines was the following:

- The images were subjected to suitable denoising and thresholding operations using the freeware ImageJ (NIH), in order to get a binarised representation of the fibrous networks (see Fig. 1(a) and (b))
- As proposed previously (Orgéas et al., 2012), fibres were then properly separated (i) by estimating a 3D Euclidian distance map inside the fibrous phase from the binarised volumes, (ii) by carrying out a thresholding operation from the resulting images.
- Subsequently, the centres of mass of the fibre sections were detected for each horizontal slice along the scaffold images, as depicted in Fig. 1(c). Fibre centrelines were then imported into Matlab®, smoothed and down-sampled using spline interpolations so that each fibre was described by 500 equally-spaced points. A mean fibre diameter of 173.4 μm was measured on the 3D images of the initial configuration, and was used as an input for the FE simulations reported below. Scaffold entire geometries were then reconstructed from the centrelines considering a constant fibre diameter, by generating normal circular sections for each point along the centrelines.

This reconstruction procedure enabled labelling each fibre, and consequently the ability to characterise in the following sections its trajectory depending on the layer it is included in.

2.3. *FE simulations*

The specificities of the dedicated FE code used in the present contribution, as well as its application to the particular case of a multilayer braided scaffold, were extensively described previously (Durville, 2012; Laurent et al., 2012). Briefly, to run the simulations, each fibre of the scaffold was individually modelled by a kinematically enriched finite strain beam model accounting for cross-sectional strains within a finite geometrical transformation framework. The mechanical behaviour of the fibres was approximated by an elasto-plastic constitutive law which links the fibre scale Green–Lagrange strain tensor with the second Piola-Kirchoff stress tensor, *via* a yield function determined from experiments performed on single PLCL fibres (Laurent et al., 2012). An original procedure was used to detect the numerous contacts in the assembly of fibres, based on intermediate geometries used to create discrete contact elements and to determine the normal directions to the contact areas. This particular procedure enables a symmetrical treatment of interacting beams. Normal contact was then modelled using a regularised and adaptive penalty method, while a Coulomb's law was used to model tangential friction at the fibre–fibre contacts. The friction coefficient was set arbitrarily to 0.1: we previously observed that this coefficient did not affect substantially results reported below. To simulate the tensile test, each scaffold layer was ascribed average kinematical boundary conditions in the form of increasing vertical displacements using artificial rigid bodies that enabled the transverse rearrangement of individual fibres (Durville, 2012). The numerical convergence of this highly non-linear procedure was achieved using a Newton algorithm. Results were exported in terms of scaffold geometry at each loading step and stress and strain tensors at many points generated on the surface of individual fibres.

In the present study, two types of simulations were reported. In the first type, the initial geometries of fibres directly extracted from X-ray tomography were taken as an input of the FE calculation. In the second type, the initial braided geometry was idealised and calculated starting from an arbitrary reference configuration in which fibres interpenetrated each other (Laurent et al., 2012). This reference arbitrary configuration based on helical fibre trajectories is only computed from the fibre diameter, an initial helix radius

and pitch length of each layer (extracted from preliminary experimental data). The non-interpenetrated configuration was then gradually computed from the knowledge of the braiding pattern within each scaffold layer. This resulted in a braided configuration taken as an "idealised" initial input for the FE simulation of the tensile test. In this case, we defined initial pitch lengths for each layer (related to the braiding angle) from preliminary measurements. The fibre diameter was set to the measured value of 173.4 μm, and the scaffold length was set to 10.3 mm which corresponds to the length of the reconstructed scaffold from tomography. In order to compare the computed scaffold geometries with experimental data, we exported the fibre centrelines and interpolated their trajectories by 500 equally-spaced points using spline interpolations.

2.4. *Comparison of experimental and numerical results*

Results issued from the experimental and from the two types of simulations were first compared in terms of global tensile response, by evaluating the force–strain response in the three cases.

In addition to this comparison of global properties, several microstructure descriptors were also used to compare the evolution of scaffold geometries during this tensile test in both experimental and numerical cases. These descriptors were computed from the fibre trajectories, issued from (i) reconstruction of X-ray tomographic image volume, (ii) FE simulation with an initial configuration reconstructed from X-ray tomography and (iii) FE simulation with an idealised initial configuration.

First, we computed the scaffold longitudinal direction by considering the least square line of the fibres trajectories. The mean distance between this scaffold axis and fibre trajectories was computed, and the results for each layer were gathered and constituted what we call hereafter the layer radii. These layer radii were computed and compared for each step of the tensile test and for the three types of considered geometries. They provided an idea of the transverse contraction of the scaffold during stretching. Moreover, this scaffold transverse contraction enabled us to estimate an apparent transverse Poisson's ratio by computing the linear regression between Green–Lagrange strain in the longitudinal and radial directions for the three types of configurations. For a homogeneous transversely isotropic material subjected to uniaxial tensile test along the z axis, *i.e.* its symmetry axis, let us recall that the transverse Poisson's ratio ν is defined as: $\varepsilon_{xx} = -\nu\varepsilon_{zz}$, where x is the transverse direction.

Second, the principal fibre curvature κ (Fig. 2) was computed along each fibre trajectory, given the parametric definition $\gamma(s)$ of a fibre centreline:

$$\kappa = \gamma' \times \gamma'' / \gamma'^3$$

where the symbol $\times$ is the cross product operator and the prime denotes differentiation with respect to the parameter s. The mean fibre curvatures for each layer were then computed and compared for each step of the tensile test and for the three types of geometries considered in this study.

Third, an average braiding angle was computed by considering the mean angle between the fibre centrelines and the scaffold axis. This angle was computed from the dot product between the local unit tangent vector $\gamma'/||\gamma'||$of the fibre centreline and the scaffold axis (Fig. 3).

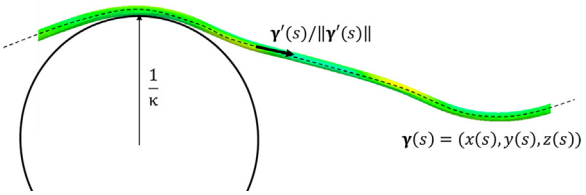

Fig. 2 – Definition of the principal fibre curvature κ of a fibre of spatial position $\gamma(s)$.

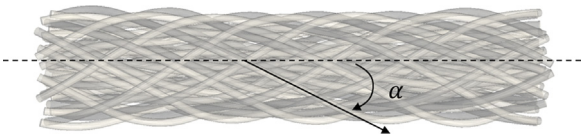

Fig. 3 – Definition of braiding angle α.

Lastly, we computed the pore size distribution within the different scaffold configurations as described in a previous study (Laurent et al., 2011). Indeed, the pore size as well as their interconnectivity and distribution in the scaffold are crucial as long as they control both the providing of cells in nutrients and the evacuation of biodegradation wastes. Briefly, a dedicated algorithm was used to generate spherical pores within the scaffold, by considering local maxima of a 3D Euclidian distance map between a point cloud and the scaffold geometry. We previously showed that this approach provided pore size distributions within the scaffold in good agreement with experimental data. Therefore, we computed the pore size distribution for each step of the tensile test and for the three types of geometries considered in the present study, and compared the resulting median pore size evolution during the tensile test.

2.5. *Computed strain at the surface of scaffold fibres*

The FE code enabled determination of the Octahedral Shear Strain *OSS* at the surface of scaffold fibres, considered here as the most influencing mechanical signal on cellular response (Lacroix et al., 2006), according to the definition:

$$OSS = \frac{2}{3}\sqrt{(\varepsilon_I - \varepsilon_{II})^2 + (\varepsilon_{II} - \varepsilon_{III})^2 + (\varepsilon_{III} - \varepsilon_I)^2}$$

where $\varepsilon_I, \varepsilon_{II}, \varepsilon_{III}$ stand for the principal strains of the fibre scale Green–Lagrange strain tensor.

These local fields were compared in the case of FE simulations computed from X-ray or idealised initial geometries, in order to assess the ability of FE simulations from idealised geometry to bring accurate information regarding the mechanical signals that will control the living cells behaviour. It is worthy to emphasise that, although *OSS* (a scalar estimator of the 3D shear stress) has been widely used in the literature and is used in the present work, it is not necessarily the best suited estimator for the surface strain that the cells will sense once adhered onto the scaffold surface.

3. Results

3.1. Overall tensile response

Experimental and simulated tensile responses from the two different initial configurations are represented in Fig. 4(a), and the experimental loading steps are clearly depicted. Whatever the considered curves (the experimental and numerical ones), a macroscale elasto-plastic response of the scaffold is systematically observed: non-linear increase of the tensile force upon loading, hysteresis during the unloading with residual tensile strain at rest. Considering the complexity of the scaffold structures, this figure also proves that FE simulations enable to satisfyingly predict the scaffold tensile behaviour, as reported previously (Laurent et al., 2012). This remark is reinforced from the 3D view proposed in Fig. 4(b): the overall experimental deformed shape is well captured by the simulations, and more precisely with the simulation initiated from the 3D images of the scaffold. However, even if the general trend is preserved, the simulations do not faithfully reproduce the unloading response of the scaffold. For the maximum scaffold stretch (step #6), the errors on predicted force are 0.2% and −5.7% for simulations using X-ray initial geometry and idealised geometry, respectively.

3.2. Transverse contraction

The evolution of layer radii during the tensile test for the three types of geometries is represented in Fig. 5. The computer radii

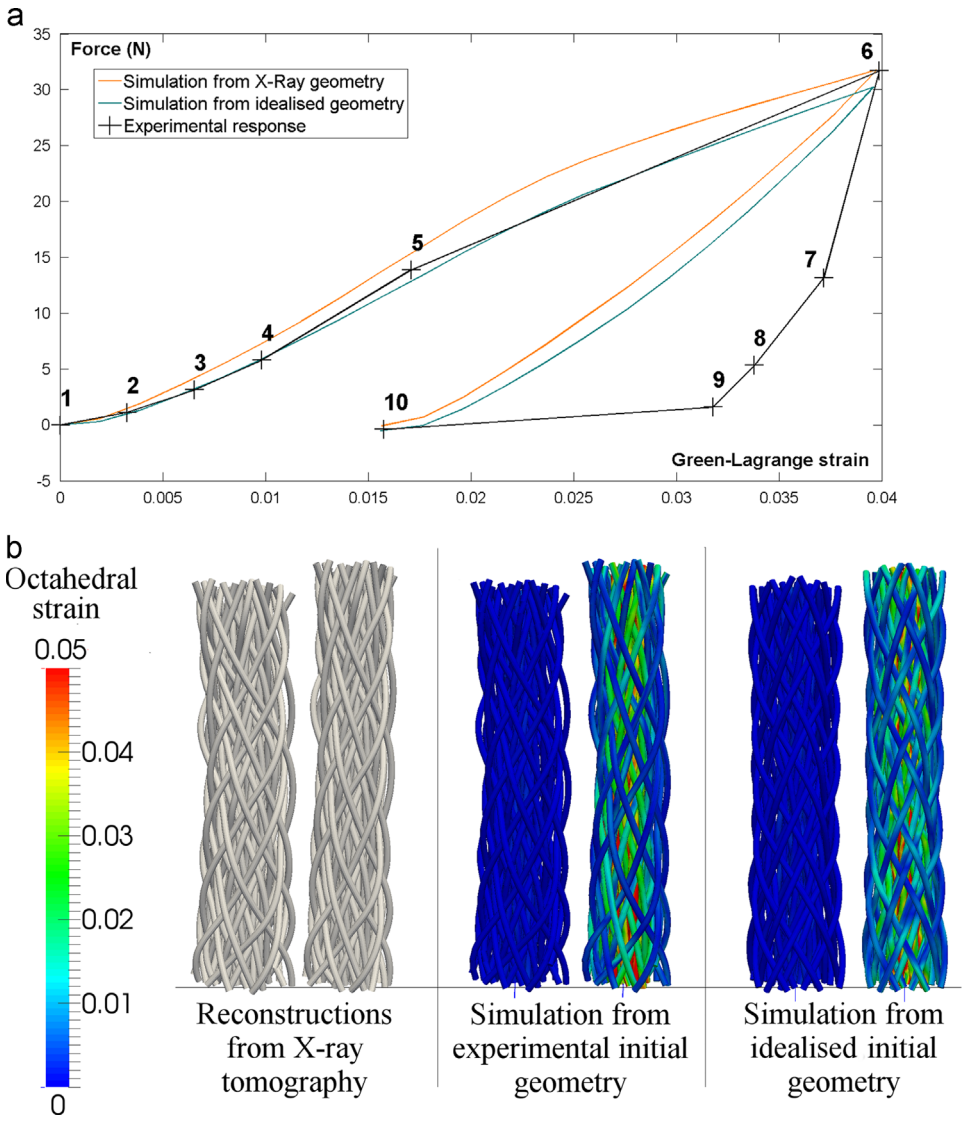

Fig. 4 – (a) Force–strain responses for the three cases considered in this study. Experimental response recorder during the X-ray tomographic acquisitions (black), simulated response with an initial configuration reconstructed from X-ray tomography (orange) or with an idealised initial configuration (green). The numbers correspond to what is called "loading step" in the manuscript. (b) Scaffold 3D geometries before stretching and at the maximum stretch in the cases of X-ray tomography reconstruction (left), FE simulations with an initial configuration reconstructed from X-ray tomography (middle), or with an idealised initial configuration (right). Colourmaps represent the values of the octahedral shear strain *OSS*. (For interpretation of the references to colour in this figure legend, the reader is referred to the web version of this article.)

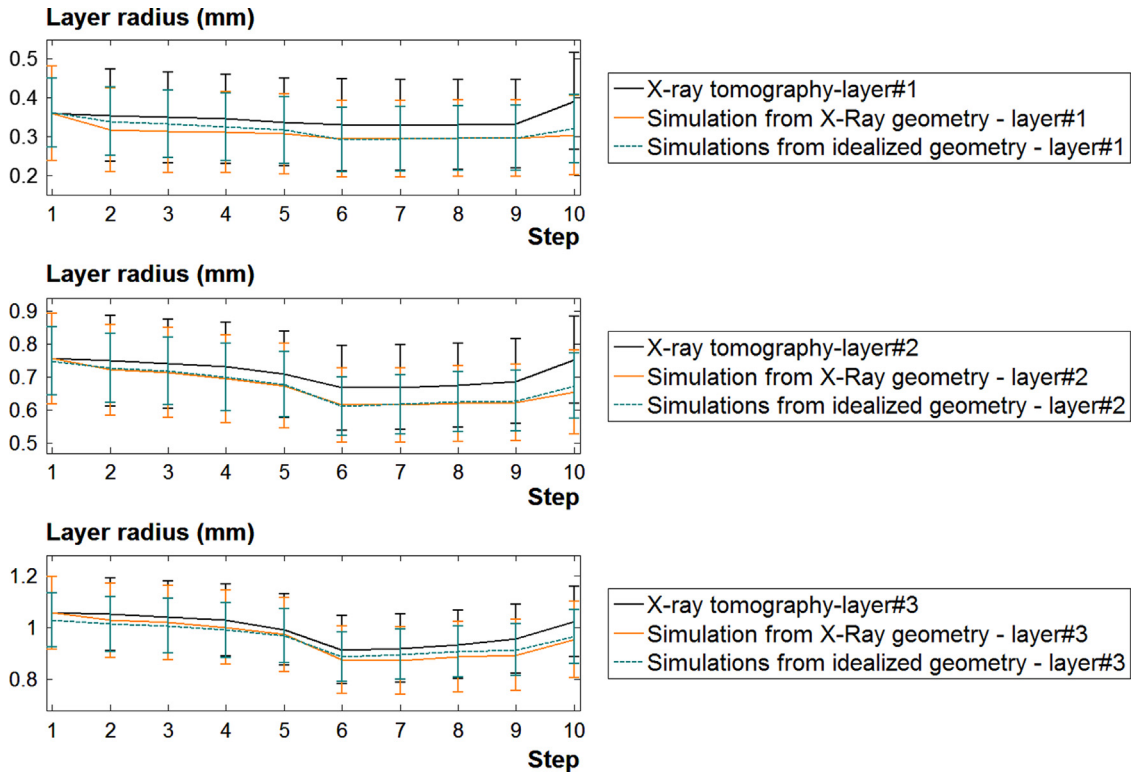

Fig. 5 – Layer radii evolution and corresponding error bars during the tensile test. Geometries issued from X-ray tomography (black), from FE simulation with an initial configuration reconstructed from X-ray tomography (orange) or from FE simulation with an idealised initial configuration (green). (For interpretation of the references to colour in this figure legend, the reader is referred to the web version of this article.)

are obviously identical for the first step in the cases of X-ray tomography and simulation from X-ray geometry. However, we clearly observed a difference from the second step and thereafter, where the geometry issued from simulation had a tendency to rearrange towards denser configurations. For the simulations from X-ray geometry, errors on layer radii at the maximal tension (step#6) are −10.8%, −7.7% and −4.2% for the layers 1, 2 and 3, respectively. For the simulations from idealised geometry, errors on layer radii at step 6 are −11.7%, −8.3% and −2.9% for the layers 1, 2 and 3, respectively. Standard deviations of radii calculation were obviously high as long as the trajectories fluctuated around the mean scaffold axis: they were around 0.11, 0.12 and 0.13 for the first, second and third layers of the X-ray tomography. Standard deviations of layer radii were lower in the simulations from idealized geometry, with values around 0.85, 0.10 and 0.10 for the first, second and third layers. Errors between the two types of simulations are below 1.5% for this step, which seems to indicate that the layer radii evolution is similar for both types of simulations.

An "apparent transverse Poisson's ratio" was computed for each configuration by considering linear regressions between longitudinal strain and radial contraction (Fig. 6). These regressions resulted in apparent Poisson's ratios of 2.99, 2.77 and 3.59 respectively for experiments, simulations from idealised geometry and simulations from X-ray geometry, with computed R^2 of 0.9943, 0.9909 and 0.9989, respectively. The radial contraction was therefore overestimated in the case of a simulation from X-ray geometry, and underestimated in the case of a simulation based on the idealised geometry. However, both simulations give the good trend.

3.3. *Fibre curvature*

The local fibre curvature was computed for each fibre of the scaffold. The evolution of mean fibre curvatures in each layer during the tensile test is reported in Fig. 7 for the three considered experimental and numerical configurations. The fibre curvature is obviously not constant along a fibre trajectory: therefore, we represented the results with error bars accounting for those variations. Proceeding like this, Fig. 7 first proves that the experimental mean fibre curvatures are well predicted with the simulation with X-ray geometry, whatever the considered layer. Besides, results obtained with an idealised geometry are also rather good, even if they slightly overestimate experimental trends for the first layer in the case of FE simulations with an idealised geometry. The maximal error on fibre curvature between experimental results and simulation with an idealised geometry reaches 32% for the loading step #6 and the first layer, while errors are much below for the two other layers.

3.4. *Braiding angle*

The evolution of the mean braiding angle per layer is plotted on the graphs of Fig. 8 for the three studied configurations.

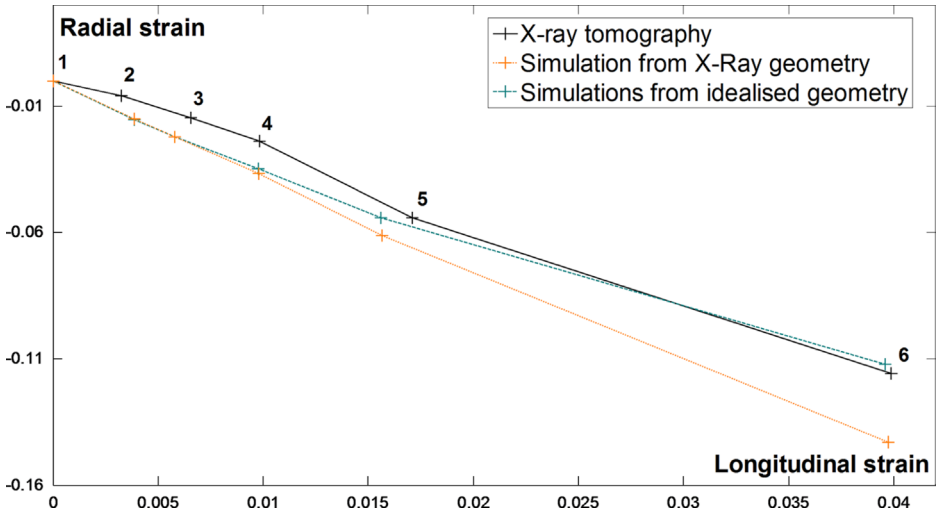

Fig. 6 – Longitudinal strain *vs* radial strain during the tensile test. Geometries issued from X-ray tomography (black), from FE simulation with an initial configuration reconstructed from X-ray tomography (orange) or from FE simulation with an idealised initial configuration (green). (For interpretation of the references to colour in this figure legend, the reader is referred to the web version of this article.)

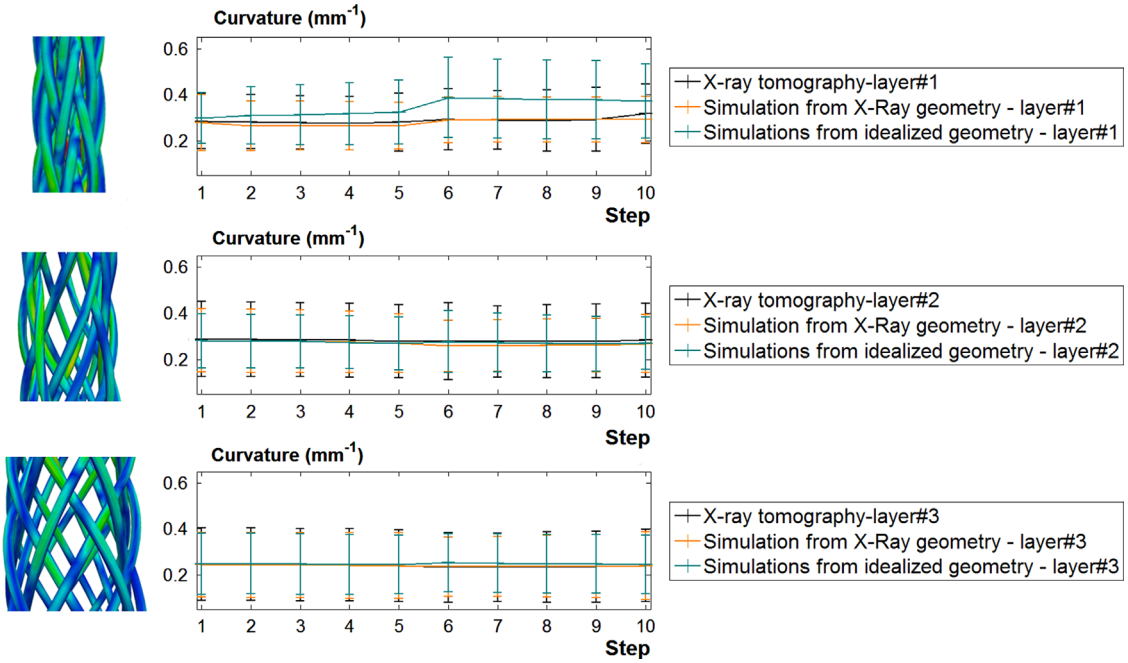

Fig. 7 – Evolution of average fibre curvature in each layer during the tensile test. Geometries issued from X-ray tomography (black), from FE simulation with an initial configuration reconstructed from X-ray tomography (orange) or from FE simulation with an idealised initial configuration (green). The pictures at the left correspond to the isolated three layers of the simulated configuration from idealised geometry (colourmap corresponds to the computed octahedral shear strain). (For interpretation of the references to colour in this figure legend, the reader is referred to the web version of this article.)

Whatever the initial numerical configuration, a very nice fit of the experimental trend is obtained from the simulations. However, as for the transverse contraction, we clearly observe a sharp fibre reorientation between the first and the second loading steps in the case of the FE simulation with X-ray initial geometry. This results in an underestimation of braiding angle with a maximal reasonable error under 10%. The braiding angle is better predicted in the case of the FE simulation with an idealised initial geometry, as long as the braiding angles of each layer in the arbitrary reference configuration used for the computation of the initial configuration are issued from experiments. A maximal error of around 7% is observed in the second layer at loading step #6. We clearly observe (Fig. 8) that the standard deviations of braiding angle is very low for the idealized geometry in comparison with the others configurations: this obviously

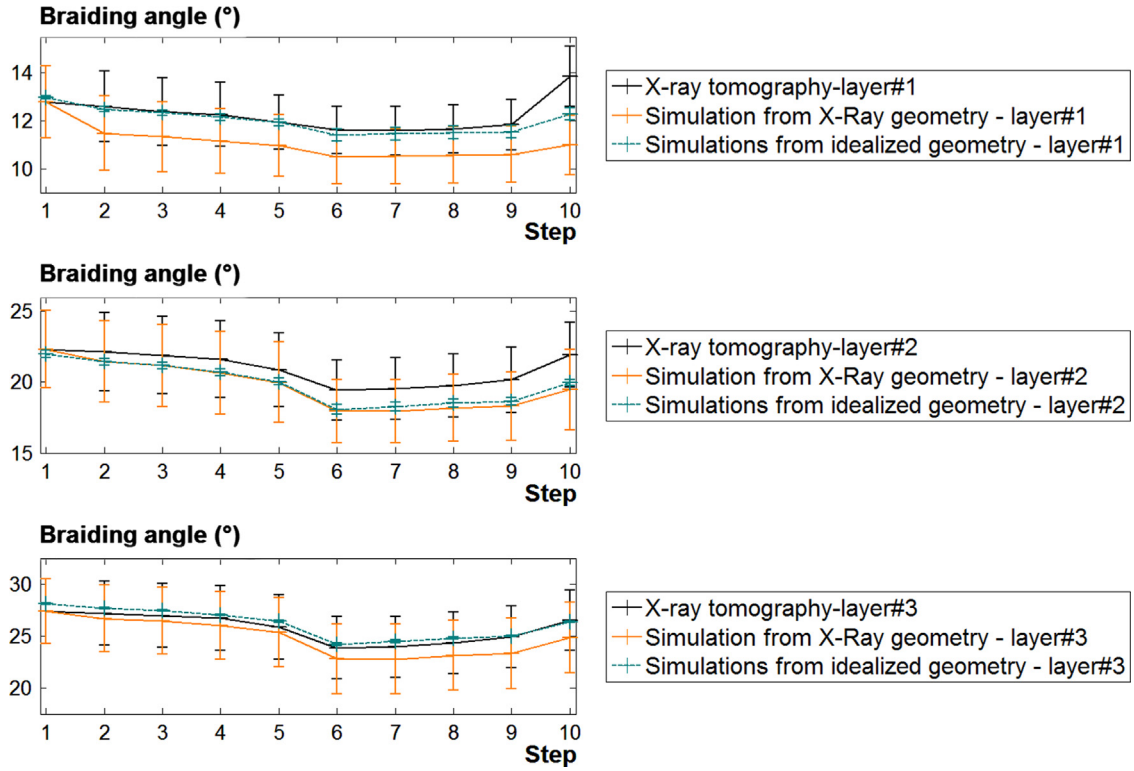

Fig. 8 – Evolution of average braiding angle α and corresponding error bars in each layer during the tensile test. Geometries issued from X-ray tomography (black), from FE simulations with an initial configuration reconstructed from X-ray tomography (orange), or from FE simulation with an idealised initial configuration (green). (For interpretation of the references to colour in this figure legend, the reader is referred to the web version of this article.)

comes from the regularity of this configuration, while fibres are more disorganised in the real geometry.

3.5. *Median pore size*

The pore size distribution was computed using previous dedicated algorithms (Laurent et al., 2011). This approach enabled to generate spherical pores within the experimental and simulated scaffolds and to compute the mean pore size evolution during the tensile test (Fig. 9). These computations show that the initial mean pore diameter is around 230 μm in the X-ray geometry and 236 μm in the idealised geometry. The pore size decreases during the tensile test, and reaches a median pore diameter of 159 μm in the X-ray geometry, 169 μm in the simulations issued from X-ray geometry, and 174 μm in the simulations issued from idealised geometry. This pore size is compatible with recommendations for ligament tissue engineering (Vieira et al., 2009). Moreover, we clearly observe (see Fig. 9) a positive pore size gradient from the scaffold core to the scaffold periphery, which has been reported to be suitable for the circulation of nutrients (Ahn et al., 2010). This explains the high standard deviations reported for pore size calculation (see Fig. 9, for instance a standard deviation 45 μm for the pore radius and the first step in the X-ray geometry). These standard deviations are very similar for the three configurations, and decrease with the tensile steps. We observe that the mean pore size is nearly constant during the unloading of the scaffold, indicating that it does not recover its original geometry. Comparable values were observed, with a slight overestimation of pore size within idealised geometries due to a more symmetrical and regular structure which enables the presence of big pores between the different scaffold layers.

3.6. *Computed strain at the scaffold surface*

FE simulations enabled to compute *OSS* at the scaffold surface, as seen on Fig. 10. Colourmaps of the computed octahedral shear strain *OSS* at the scaffold surface issued from both types of FE simulations are represented in the 3D views of Fig. 10. The associated *OSS* histograms for each scaffold layer are also reported in Fig. 11. In both cases, the *OSS* values are of the same order and the shapes of the *OSS* histograms are very similar. A clear inhomogeneity of *OSS* from the scaffold core (with high *OSS* values) to its periphery (with lower ones) is observed, constituting therefore a gradient of mechanical signals at the scale of cells that will be seeded into the scaffold which may be suitable for cellular growth. The average (±standard deviations) *OSS* for the first, second and third layer are 3.81% (±2.16%), 1.30% (±0.91%) and 0.48% (±0.41%) for the FE simulations issued from X-ray initial geometry, while in the case of idealised initial geometry they are 4.26% (±2.29%), 1.39% (±0.79%) and 0.66% (±.40%). Standard deviations are high because of the difference of *OSS* in inner or outer of a bended fibre. We therefore observe a slight overestimation of *OSS* in the case of FE simulations with an idealised initial geometry, with differences of 11%, 6% and 38% for the layers 1, 2 and 3, respectively. It is interesting to note that this

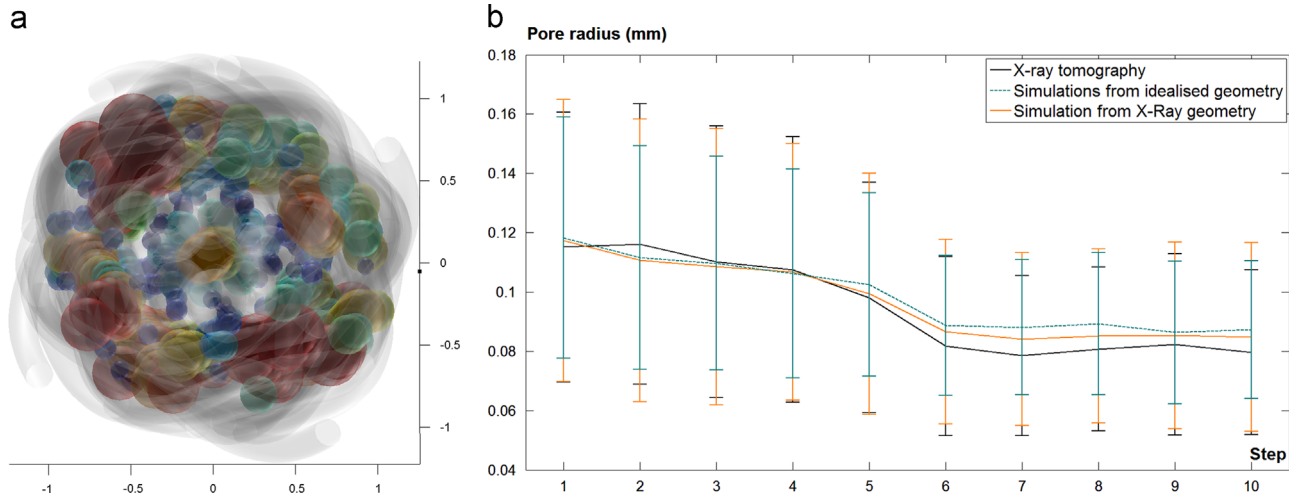

Fig. 9 – Median pore size evolution during the tensile test. (a) Generation of spherical pores within a scaffold issued from X-ray tomography. Colours correspond to pore radius. (b) Evolution of mean pore radius and corresponding error bars in the geometries issued from X-ray tomography (black), from FE simulations with an initial configuration reconstructed from X-ray tomography (orange), or from FE simulation with an idealised initial configuration (green). (For interpretation of the references to colour in this figure legend, the reader is referred to the web version of this article.)

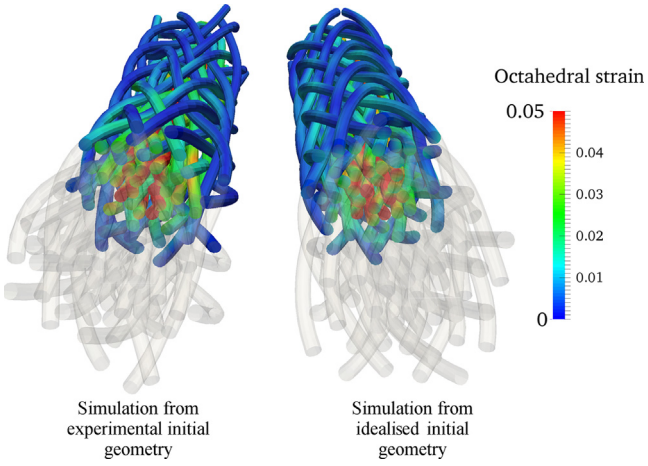

Fig. 10 – Computed octahedral shear strain at the scaffold surface in cross-sections of the scaffold. FE simulation with initial configurations reconstructed from X-ray tomography (left) or from FE simulation with an idealised initial configuration (right).

distribution of strains inside the scaffold was not particularly intuitive, which rises the interest of FE simulations to access the local mechanical fields. Indeed, in one hand, for an overall strain of around 4%, the local *OSS* rises 10% due to the heterogeneous strain distribution. In the other hand, the *OSS* is about 7 times higher in the inner layer than in the outer layer while the global strain applied to the layer is identical.

4. Discussion

Finite element simulations are increasingly used by tissue engineers in order to evaluate local mechanical signals at the scale of cells seeded into biodegradable scaffolds, and to predict and optimise the macroscopic behaviour of these scaffolds. Therefore, a validation of FE results uniquely based on the overall macroscopic response is not sufficient if one wants to use the predicted local mechanical stimuli. Within this context, the objective of the current study was thus to evaluate the results of FE simulations applied to a new braided scaffold proposed for ligament tissue engineering, by finely comparing the evolution of scaffold geometries computed from FE simulations to scaffold geometries acquired via 3D imaging during a tensile test. A characteristic of the FE code we used (Durville, 2012; Laurent et al., 2012) was the ability to compute an initial braided configuration from an arbitrary interpenetrated idealised configuration and a given braiding pattern. We therefore compared the simulated tensile test when this idealised initial geometry was used as an input geometry to the same simulated tensile test when the input geometry was issued from X-ray imaging.

X-ray microtomography has been widely used in tissue engineering in order to characterise 3D geometries of scaffolds (Moore et al., 2004), to monitor the cellular ingrowth into such scaffolds (Dorsey et al., 2009; Jones et al., 2004) or to get scaffold external geometries to serve as an input for FE simulations (Alberich-Bayarri et al., 2009). In the present study, we have used special image analysis algorithms, *i.e.* dedicated to fibrous materials, in order to extract from the 3D images proper microstructure descriptors during their deformation and to evaluate results of FE simulations with the same descriptors. The experimental challenge associated with such comparisons was twofold. First, we had to acquire the geometry of the scaffold with consideration of the individual fibres that compose the structure during a tensile test, *i.e.* by using with 3D in situ observations. Second, it was necessary to define a series of global microstructure descriptors that enable to reflect some of the relevant characteristics of the acquired and simulated geometries.

For the first point, a custom experimental set-up was designed in order to prescribe a series of tensile displacements to a biodegradable polymer and fibrous scaffold sample within

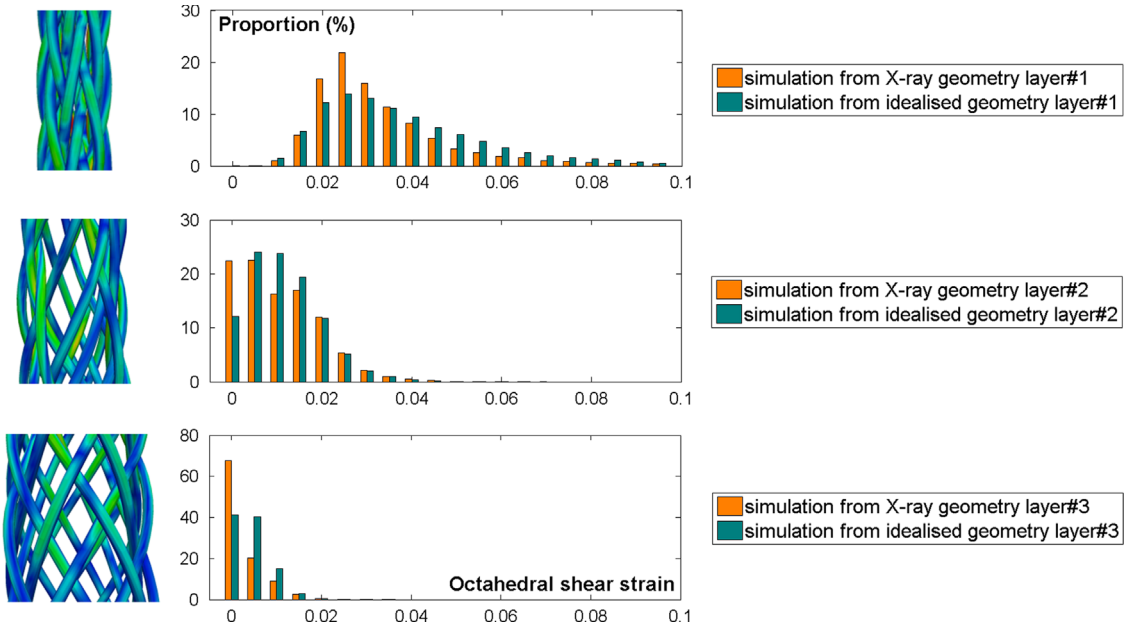

Fig. 11 – Distribution of computed octahedral shear strains at the scaffold surface for each layer. Results issued from FE simulations with X-ray initial geometry (orange) or from FE simulations with an idealised initial geometry (green). (For interpretation of the references to colour in this figure legend, the reader is referred to the web version of this article.)

a X-ray laboratory microtomograph. Combined with image processing algorithms it enabled the characterisation of the evolution of fibre trajectories during a tensile test at the different prescribed strains successively recorded upon the scaffold loading and unloading.

Concerning the comparison criteria used to compare experimental and simulated data, we initially started by comparing the experimental tensile response measured during tomographic acquisition with the simulated responses, when both idealised or X-ray geometries were taken as initial configurations for the boundary value problems to be solved with the FE code. This comparison has confirmed that the dedicated FE code used in this study enables to fairly well reproduce the tensile response of the braided scaffold to increasing load, no matter if idealised or X-ray geometries were used as inputs of the FE code. However, the unloading of the scaffold was not accurately predicted by the FE code. This point may be attributed to the constitutive law which has been considered in the FE simulations, which does not take into account viscoelasticity and loading history of the material. Indeed, the experimental procedure lasted more than one hour, and local creep or stress relaxation phenomena were necessarily present, which may have slightly changed the scaffold mechanical behaviour compared to FE simulations that ignored viscous phenomena. Moreover, we can also partly attribute these differences to the boundary conditions prescribed numerically, which could enable transverse rearrangement of individual fibres at the scaffold extremities, while it was not the case experimentally. It may have played a role on the scaffold's ability to "open" its structure during the unloading.

We then focused on the ability of the two types of FE simulations to reproduce the radial contraction of the structure during a tensile test and the evolution of fibre curvatures and braiding angle. Indeed, no descriptors such as fibre stretch could have been used, as long as the acquisition window did not follow the scaffold stretch during the tensile test. It has been found that, given the complexity of the considered structure, there was globally a satisfying concordance between these quantities extracted from tomographic data and simulation results and their evolution during a tensile test. However, these comparisons have also enabled to emphasise some discrepancies that may be explained by several factors. First, we have clearly observed a fibre rearrangement from the second loading step when the initial X-ray geometry was used as an input of the FE code, which involves that the mechanical equilibrium was not fully achieved in this geometry. This comes from the fact that a constant fibre diameter was assumed when the 3D fibres were reconstructed from the description of their centrelines, while the custom process we used in order to extrude biopolymer fibres did not enabled a strictly constant diameter. Thus, some scaffold fibres were penetrating each other in this initial geometry, which was corrected in the FE simulations due to the adaptive penalty method. This suggests that further developments should be brought to the custom plastic extruder developed to process these fibres in order to get a more homogeneous fibre diameter. This error on fibre diameter may yield to an overestimation of the radial contraction and an underestimation of the braiding angles of each scaffold layer. Despite of these differences, the present contribution suggests that regarding the complexity of the considered structure, a satisfying prediction of the scaffold geometry may be obtained by using dedicated FE simulations.

We also computed the median pore size evolution within the different types of scaffold geometries during the tensile test. We found comparable values of pore size and comparable evolutions during the tensile test, with a tendency to overestimate pore size in the case of an idealised structure due to its regular structure. Interestingly, we observed that

the initial pore size was not recovered after the unloading. It may be explained by different factors, or more likely a combination of them: (i) the prescribed loading resulted in local irreversible deformations, and the unloading therefore involved a slight compression and opening of the structure. Cyclical loading may enable to quantify this effect. (ii) Fibres exhibit creep during the test, and therefore the scaffold was in a compression state during the unloading phase. An additional image of the scaffold several minutes after the unloading could have helped to quantify the scaffold recovering. (iii) Fibres substantially rearranged during the tensile test, and therefore led to a different structure after the loading. It may therefore have been suitable to prescribe preconditioning loading–unloading cycles before the images were acquired.

In addition to the good prediction of the scaffold geometry and overall tensile response, the FE simulations enable to compute local mechanical stimuli that are known to affect the cellular activity (*e.g.* Byrne et al., 2011; Lacroix and Prendergast, 2002). Within this objective, the advantage of considering an idealised geometry as an input of FE simulation is the ability of simulating a large variety of scaffold configurations without requiring their processing. However, it is necessary to investigate the ability of these simulations to predict local stimuli identical to those computed from FE simulations starting with an experimental initial geometry issued from 3D imaging. We therefore computed the *OSS* at the scaffold surface for both types of simulations and concluded that the distribution of local signals throughout the scaffold was very similar in both cases. Therefore, it can be inferred that the approach consisting in taken an idealised arbitrary configuration as an input of the FE code will permit in the future to satisfyingly predict the scaffold macroscopic response, the scaffold geometry and the microscopic mechanical environment of the cells that will be seeded into the scaffold.

This study is obviously limited by the fact that the experimental tensile tests as well as the simulations were performed with no consideration of the fluid environment that will be present during forthcoming cyclical *in vitro* culture. Indeed, it is likely that the presence of a fluid environment will affect the fibre constitutive law and therefore the overall scaffold response, as well as the computed local mechanical signals where a wall shear stress due to fluid circulation will be added to substrate strain. This point constitutes a promising but technically challenging perspective of our approach.

5. Conclusion

In the present study, we have initiated a valuable and original dialog between the fields of experimental and numerical characterisation of fibrous media, which should enable in the future to improve the accurate characterisation of local and global behaviour of tissue-engineering scaffolds that will be used to provide alternative reconstruction methods for ligament and tendon repair. It may be concluded from the present study that the simulations performed on our new braided polymer scaffold satisfyingly predict its local and global mechanical behaviour, and may be used in the future to optimise and quantify the scaffold properties. Particularly, a precise knowledge of the local stimuli sensed by the cells by means of simulation methods could be used so as to predict – and thus optimize – the *in vitro* culture of such scaffolds, and could give rise to promising numerical work concerning models of cellular growth within these structures.

Acknowledgments

Pierre Latil gratefully acknowledge the French National Agency (ANR) for his research grant through the research program “3D discrete ANAlysis of micromechanisms of deformation in highly concentrated FIBre suspensions” (ANAFIB, ANR-09-JCJC-0030-01). The laboratory 3SR is part of the LabEx Tec 21 (Investissements d’Avenir—grant agreement ANR-11-LABX-0030).

REFERENCES

Ahn, G., Park, J.H., Kang, T., Lee, J.W., Kang, H.-W., Cho, D.-W., 2010. Effect of pore architecture on oxygen diffusion in 3D scaffolds for tissue engineering. J. Biomech. Eng. 132, 104506.

Alberich-Bayarri, A., Moratal, D., Ivirico, J.L.E., Hernández, J.C.R., Vallés-Lluch, A., Martí-Bonmatí, L., Estellés, J.M., Mano, J.F., Pradas, M.M., Ribelles, J.L.G., Salmerón-Sánchez, M., 2009. Microcomputed tomography and microfinite element modeling for evaluating polymer scaffolds architecture and their mechanical properties. J. Biomed. Mater. Res. Part B 91B, 191–202, http://dx.doi.org/10.1002/jbm.b.31389.

Butler, D.L., Juncosa-Melvin, N., Boivin, G.P., Galloway, M.T., Shearn, J.T., Gooch, C., Awad, H., 2008. Functional tissue engineering for tendon repair: a multidisciplinary strategy using mesenchymal stem cells, bioscaffolds, and mechanical stimulation. J. Orthop. Res. 26, 1–9, http://dx.doi.org/10.1002/jor.20456.

Byrne, D.P., Lacroix, D., Prendergast, P.J., 2011. Simulation of fracture healing in the tibia: mechanoregulation of cell activity using a lattice modeling approach. J. Orthop. Res. 29, 1496–1503, http://dx.doi.org/10.1002/jor.21362.

Demanget, N., Latil, P., Orgéas, L., Badel, P., Avril, S., Geindreau, C., Albertini, J.-N., Favre, J.-P., 2012. Severe bending of two aortic stent-grafts: an experimental and numerical mechanical analysis. Ann. Biomed. Eng. 40, 2674–2686, http://dx.doi.org/10.1007/s10439-012-0618-0.

Dorsey, S.M., Lin-Gibson, S., Simon Jr., C.G., 2009. X-ray microcomputed tomography for the measurement of cell adhesion and proliferation in polymer scaffolds. Biomaterials 30, 2967–2974, http://dx.doi.org/10.1016/j.biomaterials.2009.02.032.

Durville, D., 2012. Contact-friction modeling within elastic beam assemblies: an application to knot tightening. Comput. Mech 49, 687–707, http://dx.doi.org/10.1007/s00466-012-0683-0.

Jones, A.C., Milthorpe, B., Averdunk, H., Limaye, A., Senden, T.J., Sakellariou, A., Sheppard, A.P., Sok, R.M., Knackstedt, M.A., Brandwood, A., Rohner, D., Hutmacher, D.W., 2004. Analysis of 3D bone in growth into polymer scaffolds via micro-computed tomography imaging. Biomater. Focus Biomater. Sci. Aust. 25, 4947–4954, http://dx.doi.org/10.1016/j.biomaterials.2004.01.047.

Lacroix, D., Chateau, A., Ginebra, M.-P., Planell, J.A., 2006. Micro-finite element models of bone tissue-engineering scaffolds.

Biomaterials 27, 5326–5334, http://dx.doi.org/10.1016/j.biomaterials.2006.06.009.

Lacroix, D., Prendergast, P.J., 2002. A mechano-regulation model for tissue differentiation during fracture healing: analysis of gap size and loading. J. Biomech. 35, 1163–1171, http://dx.doi.org/10.1016/S0021-9290(02)00086-6.

Latil, P., Orgéas, L., Geindreau, C., Dumont, P.J.J., Rolland du Roscoat, S., 2011. Towards the 3D in situ characterisation of deformation micro-mechanisms within a compressed bundle of fibres. Compos. Sci. Technol 71, 480–488, http://dx.doi.org/10.1016/j.compscitech.2010.12.023.

Laurent, C.P., Durville, D., Mainard, D., Ganghoffer, J.-F., Rahouadj, R., 2012. A multilayer braided scaffold for anterior cruciate ligament: mechanical modeling at the fiber scale. J. Mech. Behav. Biomed. Mater. 12, 184–196, http://dx.doi.org/10.1016/j.jmbbm.2012.03.005.

Laurent, C.P., Durville, D., Vaquette, C., Rahouadj, R., Ganghoffer, J.-F., 2013. Computer-aided tissue engineering: application to the case of anterior cruciate ligament repair. Biomech. Cells Tissue, 1–44.

Laurent, C.P., Ganghoffer, J.-F., Babin, J., Six, J.-L., Wang, X., Rahouadj, R., 2011. Morphological characterization of a novel scaffold for anterior cruciate ligament tissue engineering. J. Biomech. Eng. 133, 065001.

Laurent, C.P., Vaquette, C., Martin, C., Guedon, E., Wu, X., Delconte, A., Dumas, D., Hupont, S., Isla, N.D., Rahouadj, R., Wang, X., 2014. Towards a tissue-engineered ligament: design and preliminary evaluation of a dedicated multi-chamber tension–torsion bioreactor. Processes 2, 167–179, http://dx.doi.org/10.3390/pr2010167.

Leong, N.L., Petrigliano, F.A., McAllister, D.R., 2013. Current tissue engineering strategies in anterior cruciate ligament reconstruction. J. Biomed. Mater. Res. Part Ahttp://dxdoi.org/10.1002/jbm.a.34820.

Moore, M.J., Jabbari, E., Ritman, E.L., Lu, L., Currier, B.L., Windebank, A.J., Yaszemski, M.J., 2004. Quantitative analysis of interconnectivity of porous biodegradable scaffolds with micro-computed tomography. J. Biomed. Mater. Res. Part A 71A, 258–267, http://dx.doi.org/10.1002/jbm.a.30138.

Orgéas, L., Dumont, P.J.J., Vassal, J.-P., Guiraud, O., Michaud, V., Favier, D., 2012. In-plane conduction of polymer composite plates reinforced with architectured networks of copper fibres. J. Mater. Sci. 47, 2932–2942, http://dx.doi.org/10.1007/s10853-011-6126-z.

Rathbone, S.R., Glossop, J.R., Gough, J.E., Cartmell, S.H., 2012. Cyclic tensile strain upon human mesenchymal stem cells in 2D and 3D culture differentially influences CCNL2, WDR61 and BAHCC1 gene expression levels. J. Mech. Behav. Biomed. Mater. 11, 82–91, http://dx.doi.org/10.1016/j.jmbbm.2012.01.019.

Skardal, A., Mack, D., Atala, A., Soker, S., 2013. Substrate elasticity controls cell proliferation, surface marker expression and motile phenotype in amniotic fluid-derived stem cells. J. Mech. Behav. Biomed. Mater. 17, 307–316, http://dx.doi.org/10.1016/j.jmbbm.2012.10.001.

Vieira, A.C., Guedes, R.M., Marques, A.T., 2009. Development of ligament tissue biodegradable devices: a review. J. Biomech. 42, 2421–2430, http://dx.doi.org/10.1016/j.jbiomech.2009.07.019.

Wang, J.H.-C., Yang, G., Li, Z., 2005. Controlling cell responses to cyclic mechanical stretching. Ann. Biomed. Eng. 33, 337–342, http://dx.doi.org/10.1007/s10439-005-1736-8.